Computations of unsteady cavitating flow on wing profiles using a volume fraction method and mass transfer models.

T. Huuva[1], A. Cure[2], G. Bark[1], H. Nilsson[3]
[1]Chalmers University of Technology, Shipping and Marine Technology, 412 96 Gothenburg, Sweden,
tobias.huuva@chalmers.se, bark@chalmers.se
[2]Lund Univerisity, Fluid Dynamics, 221 00 Lund, Sweden, aurelia.cure@vok.lth.se
[3]Chalmers University of Technology, Applied Mechanics, 412 96 Gothenburg, Sweden, hani@chalmers.se

Abstract

Cavitation can be modelled with a wide spectrum of methods, ranging from simple potential flow methods to highly resolved multi phase flow simulations. In this work a transport equation for the liquid/vapour volume fraction is integrated into the Implicit Large Eddy Simulation (ILES) equations, giving a highly resolved and time accurate solution strategy. Two mass transfer models, also called cavitation models, are incorporated as source terms to model the transfer of mass from liquid to vapour and back. The mass transfer models used in the present work are inspired by the works of Kunz and Sauer. These two models are based on different physical background, but the resulting equations are relatively similar. A modification of the Sauer mass transfer model is proposed, where the cavitation nuclei distribution is obtained from a separate Lagrangian Particle Tracking (LPT) simulation. Two test cases are used for the validation of the Kunz and Sauer mass transfer models, a two dimensional (2D) NACA0015 hydrofoil and a three dimensional (3D) twisted hydrofoil, the Twist11.

The 2D NACA0015 case is primarily used for testing of parameters, such as the influence of the grid resolution, the mass transfer models and the numerical interpolation schemes. Yet the results show that the computational model captures many of the features seen in the experiments, such as reentrant jets and periodic shedding. The 3D Twist11 case is a very demanding test case with many flow phenomena of interest, such the side entrant jets, which results in a closure at the centerplane, this leads to a cavity that is caught in a hairpin vortex which is transported into the wake and a reentrant jet which cuts of the sheet cavity at the leading edge. These are all features that the models are able to resolve, and the simulations thus give a realistic cavitation pattern. The representation of the side- and reentrant jets are very important to obtain a physical shedding mechanism. If the shedding is precisely represented and the early development of the cavity is correctly modelled, experience and knowledge from earlier cavitation experiments can be used to evaluate the risk of erosion.

Introduction

Cavitation can occur in a wide range of liquid flows and this complex phenomenon is not yet fully understood. Experimental observations can show many of the phenomena occurring, but together with highly accurate numerical predictions the full picture of cavitation will be much clearer. Indeed the understanding of the cavitation phenomena and the ability to predict cavitation are crucial to prevent or reduce its effects, such as damages and performance alterations. Consequently numerical prediction of cavitation is of great interest from an engineering point-of-view, especially for the hydraulic and marine industry.

Predicting cavitation is difficult partly because the physical properties of the fluid are unknown and these may vary randomly. To be able to overcome this difficulty, a high resolution simulation of the two phase flow can be used in combination with mass transfer models based on varying physical properties. In this work we study the behaviour of two different mass transfer

models for the prediction of cavitation inception and transport, where the interface between the water and the vapour is tracked using a Volume of Fluid (VOF) approach [9]. In addition a first modification is proposed to one of the mass transfer models, based on a Lagrangian Particle Tracking (LPT) [2] method where the cavitation inception is enhanced by the presence of small bubbles of air or contamination particles. Both the air bubbles and the contamination particles may act as cavitation nuclei and increase the risk of cavitation. It is thus important to understand how these particles and air bubbles are distributed in the flow field and especially in low pressure regions near the wing. In this work an Implicit Large Eddy Simulation (ILES) [7] technique is used for the handling of the turbulent flow and the VOF method describes the ratio between the content of water and vapour at every position in the flow. The volume fraction, $\gamma(x,t)$, is a scalar Heaviside function, which is used to define the fluid properties by a linear relation. To also include mass transfer due to cavitation two mass transfer models are included as source terms in the continuity and volume fraction equations, the mass transfer models by Kunz *et al.* [11] and by Sauer [16].

LES and ILES are founded on a separation of scales within the flow, accomplished by a low-pass filtering of the Navier Stokes Equations (NSE) [15]. Large energy containing structures that can be resolved by the computational grid are predicted in the LES calculation, whereas the smaller, more isotropic turbulent structures are modelled. This gives LES a much higher generality than e.g. Reynolds Averaged Navier Stokes (RANS) [21] in which the complete spectrum of turbulent motion is modelled. Furthermore LES preserves more of the physics which can be useful in cavitation simulation. Earlier Wikström *et al.* [19,20] and Persson *et al.* [14] has presented work on ILES in combination with cavitation modelling and Wosnik *et al.* [22] has presented work with LES and cavitation modelling.

The presented models are tested on two different wing profiles, one with a two dimensional (2D) profile and one with a three dimensional (3D) profile. The 2D profile is a NACA0015 profile, which is a relatively thick wing section, at 8 degree angle of attack. In this configuration a sheet cavity starts from the leading edge and this sheet grows until a reentrant jet forms and cuts it off. In addition a twisted wing is tested, referred to as Twist11, described by Foeth and Terwisga [3], in which phenomena not present on a 2D foil occurs. An example of such a flow phenomenon is the sidentrant jets which cut the sheet and form a closure from which a cavity in a hairpin vortex is convected. The sideentrant jets then forms into a reentrant jet which cuts the cavity at the leading edge.

Modelling

Flow modelling

The governing equations of an incompressible flow consist of the balance equations of mass and momentum (Navier-Stokes Equations, NSE) for a linear viscous (or Newtonian) fluid [13],

$$\partial_t(\mathbf{v}) + \nabla\cdot(\mathbf{v}\otimes\mathbf{v}) = -\nabla \mathrm{p} + \nabla\cdot\mathbf{S}, \quad \nabla\cdot\mathbf{v} = 0, \tag{1}$$

where v is the velocity, p is the pressure, S=2νD is the viscous stress tensor, $\mathbf{D} = \frac{1}{2}(\nabla\mathbf{v} + \nabla\mathbf{v}^T)$ is the rate-of-strain tensor and ν is the kinematic viscosity. Resolving all structures in the flow field, i.e. solving the full NSE, is referred to as Direct Numerical Simulation (DNS). This implies solving for the smallest scales in flow, the Kolmogorov scale, and this gives a computational time which will scale as Reynolds number (Re) cube. This results in a too long computational time for present-day computers, even for model scale. DNS may however still be useful for analyzing

academic flows to gain detailed insight in the flow physics. The alternatives to DNS all involve some degree of modelling; here Implicit LES (ILES) is used. In the ILES approach the effects of the subgrid physics on the unresolved scales are incorporated in the functional reconstruction of the fluxes using high-resolution finite-volume methods. The spatial discretization effectively filters the NSE over the grid using an anisotropic top-hat shaped kernel, providing the implicitly filtered and discretized equations. These are closed by specific flux reconstruction schemes applied to the convective and viscous fluxes. In the viscous fluxes the inner gradient is usually evaluated using central differencing (as in LES) and similarly, linear reconstruction is used to finalize the discretization of these.

Cavitation modelling

The cavitation models used in this work are based on different backgrounds and physical properties, but a common problem is that all models introduce constants that are assessed by comparisons with experimental results. These empirical constants are not universal and they depend on the geometry and the flow conditions. It is consequently of great importance to compare the models using a common implementation of the CFD solver and using a simple geometry where the numerical predictions can be compared with experimental observations.

We will here refer to the cavitation modelling as mass transfer models for cavitating liquids, since that is what the models are actually about. It is not possible to resolve the mass transfer in a continuum representation and consequently mass transfer modelling is needed. The cavity in itself is not modelled, since it is present in the simulation, and it would then be confusing to refer to the models as cavitation models. If a true cavitation modelling would be performed, no cavity would be present in the simulation and the purpose of the cavitation model would be to account for the influence of the cavity on the main flow. In the present computations the cavity appears as a part of the basic ILES equations, i.e. as a part of the steady flow field, when the ILES equations are solved together with the mass transfer model, producing vapour inside the liquid when the pressure is below the vapour pressure. Although the production and destruction of vapour, described by the mass transfer model, is a crucial part of the cavitation process, other parts as reentrant jets and shedding being the main subject below, are controlled rather by the ILES equations. We therefore mean here by a cavitation model the entire set of equations solved to describe the flow. This nomenclature is motivated by the fact that changes of the basic flow solver can be of same importance, at least, as changes of the mass transfer model.

Using the VOF approach a transport equation for the volume fraction needs to be incorporated into the filtered balance equations of mass and momentum (1)

$$\begin{cases} \nabla\cdot\overline{\mathbf{v}} = 0, \\ \partial_t(\rho\overline{\mathbf{v}}) + \nabla\cdot(\rho\overline{\mathbf{v}}\otimes\overline{\mathbf{v}}) = -\nabla\overline{p} + \nabla\cdot(\overline{\mathbf{S}} - \mathbf{B}), \\ \partial_t\gamma + \overline{\mathbf{v}}\cdot\nabla\gamma = 0. \end{cases} \tag{2}$$

where $\mathbf{B}=(\overline{\mathbf{v}\otimes\mathbf{v}}-\overline{\mathbf{v}}\otimes\overline{\mathbf{v}})$ is the subgrid stress tensor arising from the filtering, see e.g. Fureby *et al.*[6] for clarification, and the volume fraction is used to scale the physical properties vapour and the liquid

$$\begin{cases} \rho = \gamma\rho_l + (1-\gamma)\rho_v, \\ \mu = \gamma\mu_l + (1-\gamma)\mu_v, \end{cases} . \tag{3}$$

The numerical behaviour of the volume fraction equation can be treated in several different ways, using high and low order, compressive and non-compressive reconstruction schemes for the convection of the volume fraction [18].

Kunz mass transfer model for cavitating liquids

Kunz' mass transfer model for cavitating liquids is based on the work by Merkel *et al.* [12], with a modification which corresponds to the behaviour of a fluid near the transition point. The behaviour near a transition point is described by methods within statistical physics and the inventors of the model refer to the Ginzburg-Landau potential [10] and van der Waals equation of state [8], as the basic physics. The mass transfer in this model is based on two different strategies, as compared to most similar models which only rely on one strategy for both creation and destruction of liquid. The destruction of liquid, or creation of vapour $\dot{m}^+$, is modelled to be proportional to the amount by which the pressure is below the vapour pressure and the destruction of vapour $\dot{m}^-$ is based on a third order polynomial function of the volume fraction $\gamma = \frac{Volume\,liquid}{Total\,Volume}$

$$\begin{cases} \dot{m}^+ = \left(C_{prod}\rho_v / \rho_l U_\infty^2 t_\infty\right)\cdot \gamma \min[0, \bar{p} - p_v], \\ \dot{m}^- = \left(C_{dest}\rho_v / t_\infty\right)\cdot \gamma^2(1-\gamma). \end{cases} \tag{4}$$

where $\dot{m} = \dot{m}^+ + \dot{m}^-$ is the specific mass transfer rate, $\bar{p}$ is the filtered pressure, p_v is the vaporisation pressure, ρ is the density and $C_{dest}, C_{prod}, U_\infty$ and t_∞ are empirical constants based on the mean flow. The mass transfer terms are incorporated into the flow modelling using source terms in the continuity equation and in the transport equation for the volume fraction,

$$\begin{cases} \nabla\cdot\bar{\mathbf{v}} = S_\rho, \\ \partial_t(\rho\bar{\mathbf{v}}) + \nabla\cdot(\rho\bar{\mathbf{v}}\otimes\bar{\mathbf{v}}) = -\nabla\bar{p} + \nabla\cdot(\bar{\mathbf{S}} - \mathbf{B}), \\ \partial_t\gamma + \bar{\mathbf{v}}\cdot\nabla\gamma = S_\gamma. \end{cases} \tag{5}$$

here S_ρ and S_γ are the mass transfer source terms. For a volumetric source representation, S_ρ can be expressed as,

$$S_\rho = \dot{m}(\rho_l^{-1} - \rho_v^{-1}), \tag{6}$$

where $(\rho_l^{-1} - \rho_v^{-1})$ handles the bulk volume change when mass is transferred from one phase to the other. The bulk density for liquid and vapour, ρ_l and ρ_v, are kept constant throughout the computation. The source term in the volume fraction transport equation, S_γ, can be estimated from the mass transfer from vapour to liquid at a rate $\dot{m}$. The bulk density change rate can be represented as,

$$D_t(\rho) = -\rho\nabla\cdot\bar{\mathbf{v}} \tag{7}$$

and as

$$D_t(\rho) = (\rho_l - \rho_v)D_t(\gamma). \tag{8}$$

using equation (3_1). Combining equations (7) and (8) and rearranging the terms gives the volume fraction equation as

$$D_t\gamma + \nabla\cdot\left(\bar{\mathbf{v}}\gamma\right) = -\frac{\rho_l}{\rho_v - \rho_l}\nabla\cdot\bar{\mathbf{v}}\,. \tag{9}$$

Sauer's mass transfer model for cavitating liquids

In contrast to Kunz' model, the background to Sauer's mass transfer model [16] is relatively explict and can be described in a few lines. Sauer's model is based on bubble dynamics and the amount of vapour in a control volume is calculated from the number of nesting vapour bubbles and an average radius of these bubbles. The dynamic of the bubbles is governed by the Reyleigh equation

$$R\frac{\partial^2 R}{\partial t^2} + \frac{3}{2}\left(\frac{\partial R}{\partial t}\right)^2 = \frac{p(R) - p_\infty}{\rho_l}\,, \tag{10}$$

this equation is however simplified by neglecting the second-order derivative. The use of this model, with simplifications for bubble dynamics is discussed and justified in Sauer [16]. Solving for the derivative of the bubble radius gives the growth rate as

$$\frac{dR}{dt} = \sqrt{\frac{2}{3}\frac{p(R) - p_\infty}{\rho_l}}\,. \tag{11}$$

To incorporate the bubble dynamics into the flow equations, the source term in the continuity equation (5_1) can be written as

$$S_\rho = \frac{1}{\rho}\frac{\partial\rho}{\partial t}, \tag{12}$$

using the continuity equation for an incompressible fluid with density gradients

$$\frac{\partial\rho}{\partial t} + \nabla\cdot\rho\,\bar{\mathbf{v}} = 0 \tag{13}$$

and the fact that there will not be any velocities across the density gradient. By using equation (3_1) and the fact that $(\rho_v << \rho_l)$ the source term can be rewritten as

$$S_\rho = \frac{1}{1-\alpha}\frac{\partial\alpha}{\partial t}. \tag{14}$$

The volume fraction $\alpha = \frac{Volume\,vapour}{Total\,Volume}$, used here, is expressed, in contrast to γ in kunz' model, as the ratio between the vapour in a control volume and the total volume of the control volume, giving

$$\alpha = \frac{n_0 \frac{4}{3}\pi R^3}{1 + n_0 \frac{4}{3}\pi R^3}, \tag{15}$$

where n_0 is the number density, i.e number of bubbles per volume unit, and R is the average radius of these bubbles. Inserting equation (15) into equation (14) and rearrange gives the source term as

$$S_\rho = \frac{3\alpha}{R}\frac{\partial R}{\partial t}, \tag{16}$$

into which equation (11) can be inserted, giving

$$S_\rho = \frac{3\alpha}{R} sign(p_v - p)\sqrt{\frac{2}{3}\frac{|p_v - p|}{\rho_l}}, \tag{17}$$

here the pressure at the bubble surface is replaced by the vapour pressure and p is replaced by the ambient cell pressure.

The source term in the volume fraction equation S_γ is found by identifying the following relationship

$$\frac{\partial \alpha}{\partial t} + \alpha \nabla \cdot \bar{\mathbf{v}} = \frac{\partial \alpha}{\partial t} + \alpha \frac{1}{1-\alpha}\frac{\partial \alpha}{\partial t} = \frac{1}{1-\alpha}\frac{\partial \alpha}{\partial t} = S_\rho = S_\gamma \tag{18}$$

The radius of the bubbles used in the source term can either be computed from equation (15), using a constant or pre-calculated specific bubble density n_0, giving

$$R = \sqrt[3]{\frac{\alpha}{n_0 \frac{4}{3}\pi(1-\alpha)}}, \tag{19}$$

or by solving a transport equation for the bubble radius using equation (11) and an initial bubble radius R_0. The results presented here are primarily computed using equation (19) with a constant value of the specific bubble density.

Sauer's mass transfer model with a varying bubble density

As an alternative of using a constant value for n_0 in Sauer's mass transfer model, a pre-calculated specific bubble density is a first step towards a more integrated approach where the estimation of the bubble density and the cavitation modelling is performed in conjunction. Here we intend to use a Lagrangian Particle Tracking (LPT) method to model and track the nuclei in the flow. A nucleus is defined by the position of its centre position $\mathbf{x}_p$, its diameter D_P, its velocity $\mathbf{U}_P$ and its density ρ_P. In the Lagrangian frame of reference each particle position vector is calculated from the equation $\frac{d\mathbf{x}_p}{dt} = \mathbf{U}_P$ and the motion of the particles is governed by Newton's equation $m_P \frac{d\mathbf{U}_P}{dt} = \sum \mathbf{F}$. The dominant force acting on the particle is the drag $\mathbf{F_D}$ from the fluid phase given by

$$\mathbf{F_D} = \frac{3}{4}\frac{m_P}{\rho_P D_P}\rho C_D|\bar{\mathbf{v}} - \mathbf{U_P}|(\bar{\mathbf{v}} - \mathbf{U_P}) \quad (20)$$

where the drag coefficient C_D is given by

$$C_D = \begin{cases} 24\,\mathrm{Re}_P^{-1}(1 + 0.16\,\mathrm{Re}_P^{2/3}) & if\ \mathrm{Re}_P \le 1000 \\ 0.44 & if\ \mathrm{Re}_P > 1000 \end{cases}$$

and Re_P is the particle Reynolds number $\mathrm{Re}_P = \frac{\rho D_P|\bar{\mathbf{v}} - \mathbf{U_P}|}{\mu}$.

Since the fluid velocity $\bar{\mathbf{v}}$, calculated in the Eulerian frame of reference, is needed for the calculation of the drag force in the Lagrangian frame of reference, it has to be interpolated to the position of the particle from the neighbour grid points.

A one-way coupling is applied for the LPT which means that the source term due to particle-fluid interactions in the Navier Stokes equations (1) is neglected and particle-particle interaction is not consider. Collision of a particle with the wing is modelled by evaluating the particle normal velocity after collision as $U_P^{n'} = \varepsilon_w U_P^n$ where $\varepsilon_w \in [0,1]$ is the coefficient of restitution of the wall that accounts for the energy lost during the dissipative collision. The value of $\in$ is 0.2 for a bubble and 0.7 for a hard particle.

The particles are injected randomly at every time step from a vertical plane upstream the wing and the simulations are time-averaged for several through-flow times in order to achieve a statistically stationary result for the nuclei density. This time-averaged nuclei distribution will then be used as the pre-calculated specific bubble density n_0 for the Sauer model.

Validation of the NACA0015 case

Setup

In the first test case, the NACA0015, the computational results are compared with the experiments by Yakushiji [23]. The Reynolds number (Re) is 1,200,000, the cavitation number (σ) is 1.2 and the angle of attack is 8 degrees. Both models are used and the computations are performed on two different computational grids, see Fig. 1.

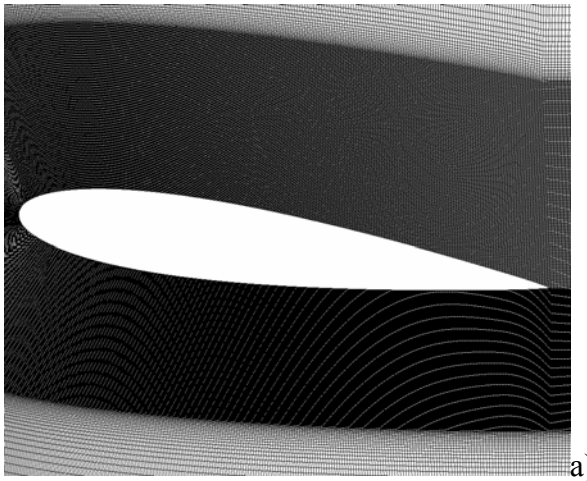
a)

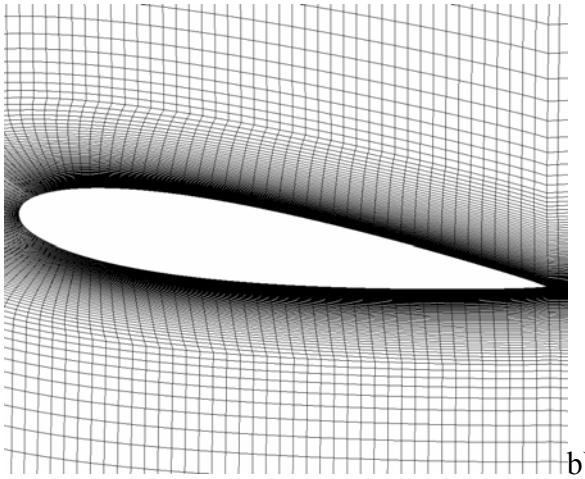
b)

Figure 1.NACA0015 8 degree angle of attack a) High resolution computational grid, 267,000 cells b) Low resolution computational grid, 21,000 cells.

The finer grid is used to study the small structures of the flow field, while the coarser grid is mainly used to study the influence of models and parameters. In the computations presented below the four constants introduced in Kunz cavitation model is used as $t_\infty = 0.1$, $U_\infty = 10$, $c\,\mathrm{Pr}od = 10^7$ and $cDest = 1$ and in Sauer's mass transfer model the specific bubble density is $n = 10^7$.

Validation

In Fig. 2a-h below a qualitative comparison between the experimental visualizations and the computational results produced on the fine mesh with Kunz mass transfer model is made. The major difference between the experimental view and the computed view is that the experiment shows a type of integrated view of the entire spanwise extension while the computations, which are two-dimensional, give the average of the spanwise direction. Consequently the experiment is only used as a qualitative comparison for some checking of the relevance of the simulated data and the main focus is put on the different models and settings presented below.

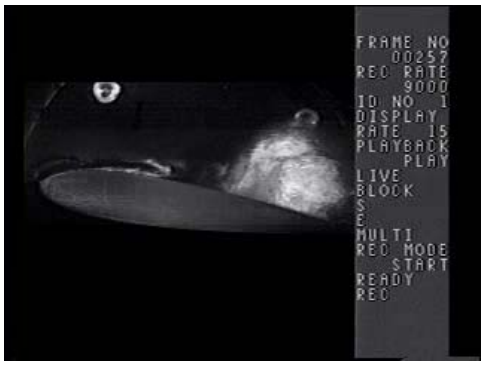

a)
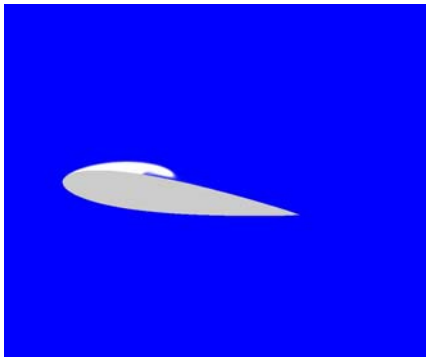
b)
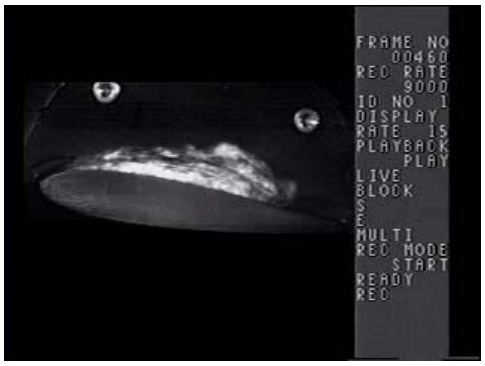

c)
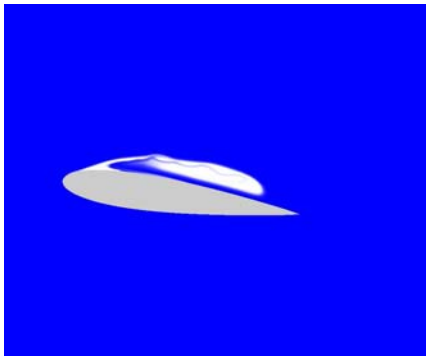
d)

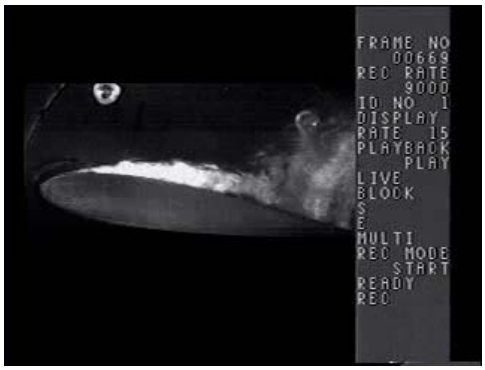

e)
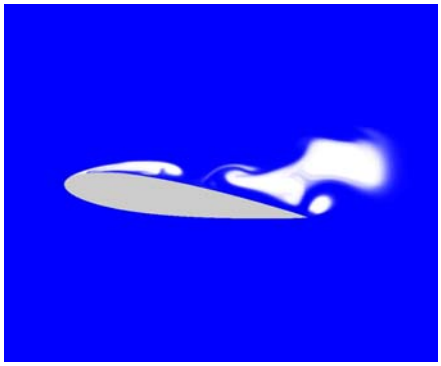
f)
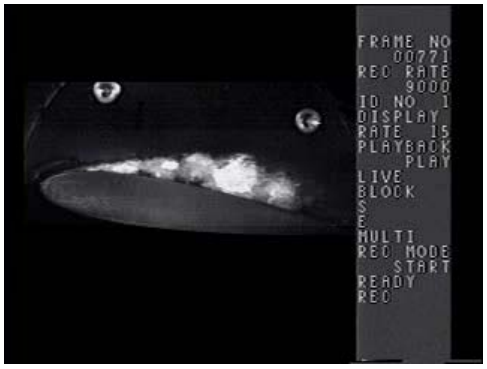

g)
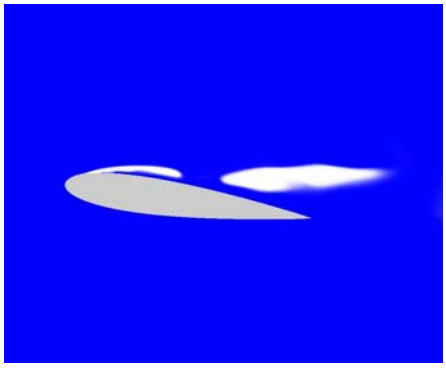
h)

Figure 2. Comparison between experiments and computations on the NACA0015 at 8 degree angle of attack. a-b) First cycle in the experiments showing the growth of the sheet cavity. c-d) The reentrant jet has almost reached the leading edge of the hydrofoil, the experiment starts to be bubbly. e-f) The first sheet is released and convected, while a new sheet cavity is growing. g-h) the second sheet is now convected and a third is growing.

In figure 2 the experiments show a sheet cavity which is started at the leading edge. This cavity is transported along surface of the hydrofoil and when it exceeds a certain size it becomes unstable and sheds cloud cavitation periodically. This process is controlled by a reentrant jet which is forming downstream of the cavity and travels in the opposite direction to the outer flow towards the leading edge. When the reentrant jet approaches the leading edge it connects with the outer flow and a strong shear occurs between the outer flow and the opposite flow in the reentrant jet. The cavity is now broken up into a cloud of smaller bubbles which is transported with the free-stream towards the trailing edge of the hydrofoil. This break-up of the cavity into a genuine cloud of bubbles is a process which the present cavitation models are not able to capture. Instead the cavitation models treat this cloud of bubbles as a combination of smaller and larger detached voids which is transported into the wake region, yet some resemblance with a real cloud may however be reflected in the γ-distribution in the shed parts. All computations presented here are performed on a 2D section of the wing, which is of course a strong limitation, but it is necessary to be able test as many conditions as possible. A 3D section, with a relatively sparse resolution in the spanwise direction has also been performed to check the differences between 2D and 3D results, but no large difference is found.

In the computations there is generally a difference between the first and the following cycles of cavities, this phenomena is expected since the first cavity is only affected by the undisturbed flow field only, while the following cycles will be affected by the disturbed velocity and pressure field from the preceding cavity. This disturbance becomes relatively large since the transported cavity remains as a sheet and is not broken up into bubbles. In experimental studies there is usually no first cavity, which can be compared with the first cavity of the computations. Yet the first cavity

in the computations is interesting to study since it demonstrate the work of the cavitation model in relatively undisturbed flow and it is in this case easier to see the direct differences between models and parameters. The first cavity is in fact also of engineering relevance in cases of inhomogeneous inflow to for example propellers.

Mass transfer models

In figures 3-6 we compare the behaviour of the two mass transfer models on the coarse mesh. More combinations of the different parameters have been studied, but are not presented here. The experience from this study shows that Kunz' cavitation model is relatively insensitive to the choice of the production constant. Generally one can see that the term should be as large as possible. However, if it is too large the computation might be instable due to the large source terms. The value of the destruction constant is more sensitive, especially in combination with the grid density. In Kunz' mass transfer model the destruction is only related to the vapour fraction. As soon as the vapour fraction is between 0 and 1 the destruction term will be active and destroy vapour, making the surface sharper. If the destruction term is large the surface of the sheet cavity will be relatively sharp, but the cavity might be destroyed to early. With a lower value of the destruction term the surface of the cavity will be diffuser and the cavity lives longer. Using Sauer's mass transfer model there is a number of ways to treat the constants. In the computations presented below the bubble radius is related to the volume fraction using a specific bubble density n_0 . This specific bubble density can either be constant or have a distribution is space. If the distribution is constant the size of the destruction and production term will be relatively equal in space. Using a distribution where the nuclei's are more densely packed close to the stagnation point and less densely packed on the suction side the production can be made larger than the destruction, which could be favourable. The third alternative is to integrate the bubble radius in time, giving smaller bubbles close to the inception point, which relates to a large production, and larger bubbles on the suction side, which consequently makes the source term smaller.

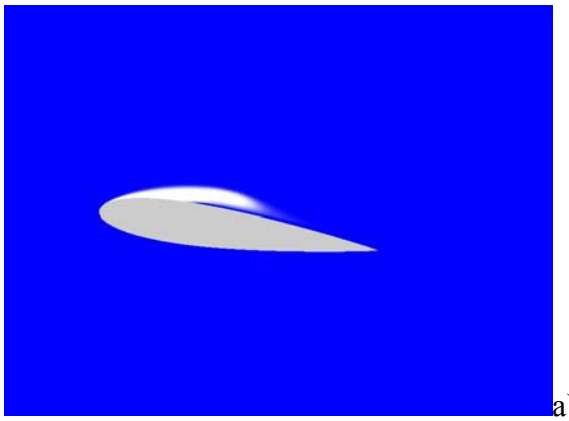
a)
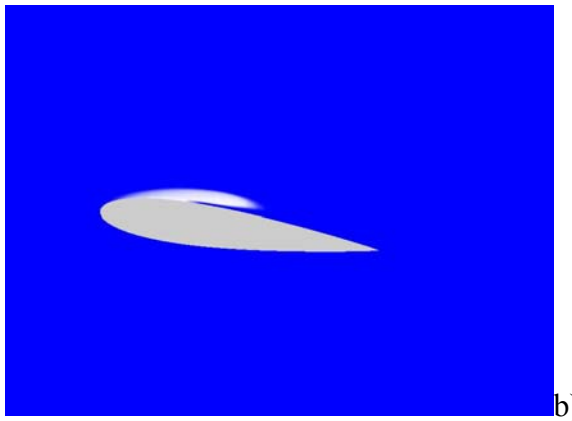
b)

Figure 3. Growth of the first cycle. a) Kunz, $c_{Prod} = 10^7$ and $c_{Dest} = 1$. b) Sauer, $n_0=10^7$.

In the first cycle, see Fig. 3, no great difference between the mass transfer models occurs. Both models demonstrate a small overshoot of the leading part of the cavity over the fluid in which the velocity of the fluid is directed in the streamwise direction. Consequently no reentrant jet is yet initiated. The inertia of the cavity will act on this fluid and make it create a reentrant jet within this flow. When the reentrant flow is initiated a stagnation point will occur behind the cavity and this stagnation point will feed the reentrant jet with fluid from the outer flow.

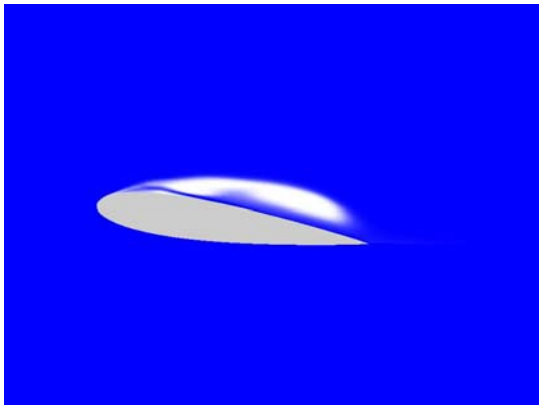
a)
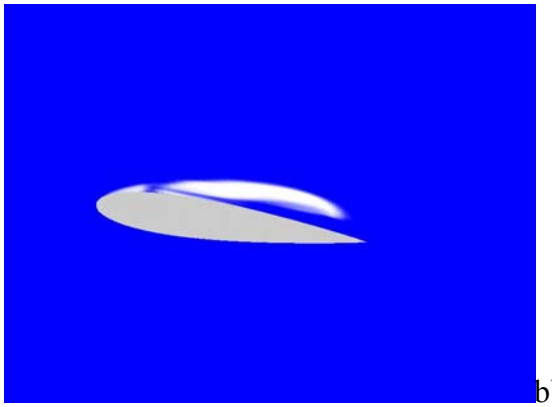
b)

Figure 4. Reentrant jet in the first cycle. a) Kunz, $c_{Prod} = 10^7$ and $c_{Dest} = 1$. e) Sauer, $n0=10^7$.

When the cavity reaches its maximum length, see Fig. 4, the difference between the computed predictions is slightly larger than in Fig. 3. A distinct difference is the amount of liquid which is located under the cavity close to the trailing edge of the wing. The liquid in this region attains a rotational movement which almost cuts of the cavity before the reentrant jet reaches the leading edge. This phenomenon is especially visible when the destruction term is large in Kunz mass transfer model (this state is not shown). Using Sauer's mass transfer model there are only very small differences between a smaller ($n_0=10^7$shown here) and a larger specific bubble density ($n_0=10^{11}$ not shown here). In both cases a thicker region of fluid is collected close to the leading part of the cavity, as in the case with Kunz' model with a large destruction term. The main difference is that the thickening is not directed towards the outer flow. Instead the whole cavity is lifted from the foil. The difference between the overall shape and thickness of the cavity between Kunz' model and Sauer's model is mainly related to the location and size of the mass transfer terms.

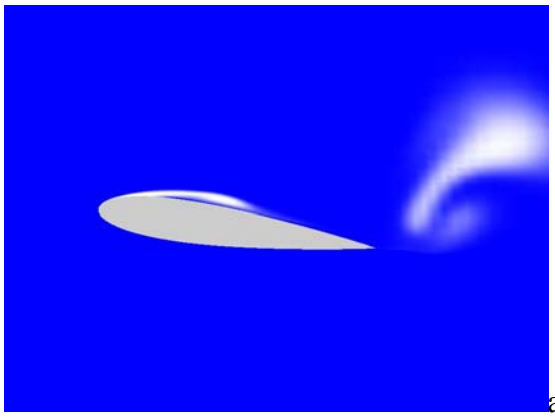
a)
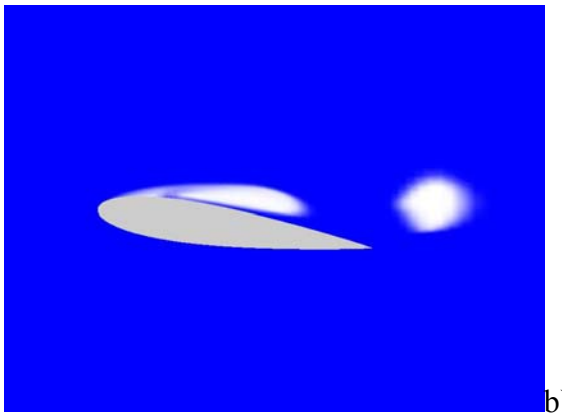
b)

Figure 5. Growth of the second cycle a) Kunz, $c_{Prod} = 10^7$ and $c_{Dest} = 1$. b) Sauer, $n_0=10^7$.

After the first cycle, in which the shedding mechanism is very similar for the different models and parameter settings, the second cycle is growing from the leading edge, see Fig. 5. This cycle is largely influenced by the transport and collapse of the previous cycle. If the destruction term is large the cavity will be destroyed rapidly which creates a favourable pressure distribution for the second cavity to develop. In this case the cavity grows faster and more distinct than the cavity which is controlled by a smaller destruction term, see Fig. 5a. An increase of the destruction term

influences the results insignificantly. This depends on the narrow band where the construction term is active, excluding areas of strong rotation where construction also appears. The construction of vapour is limited to a small part of the leading edge and as long as the water that enters this region is vaporized, the difference between the models will be small.

Results from Sauer's model show small differences between the different specific bubble densities (not shown). With a higher bubble density the cavities live slightly longer in the wake, which is expected, but the length and thickness of the attached cavity is quite similar between the two settings. Also at this time step Sauer's model has a big similarity with Kunz' model with a large destruction term.

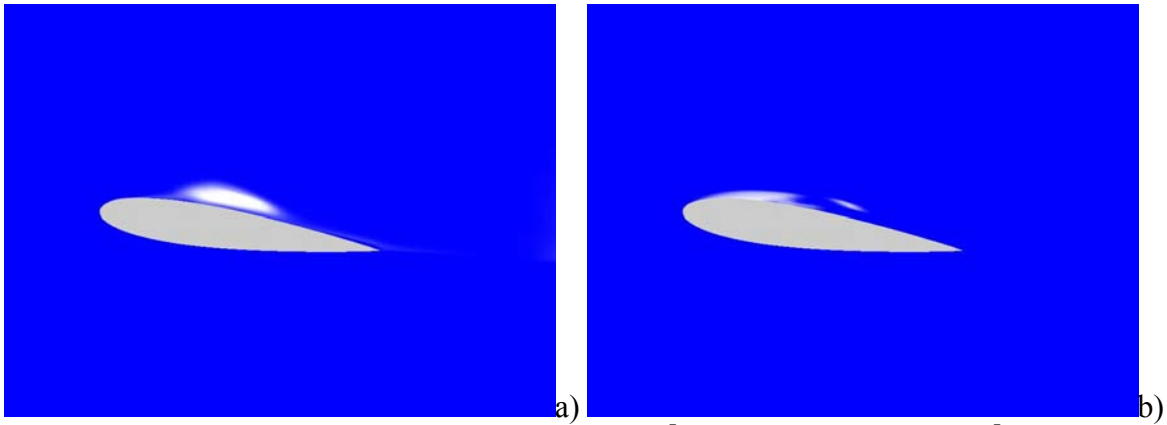

Figure 6, Reentrant jet in the second cycle. a) Kunz, $c_{Prod} = 10^7$ and $c_{Dest} = 1$. e) Sauer, $n_0=10^7$.

When the cavity in the second cycle has reached its maximum length, see Fig. 6, both settings with Sauer's model and Kunz' model with a large value of the destruction term predicts a thicker reentrant formation. The Kunz model with lower value on the destruction term still predicts a thinner reentrant jet. When the thicker reentrant jet enters the cavity it leaves a number of cavities located in small vortices which are formed by the shearing between the reentrant jet and the outer flow. These small vortices are then gathered by a larger rotational formation and become one large cavitation sheet.

By studying the sign and strength of the source term of the different models and settings the similarities can be better understood. All computations have a very narrow band close to the leading edge where a large positive source term appears, i.e. production of vapour. In Sauer's model both the area of production and the peak value is larger than in Kunz' model. This fact can probably be related to the fact that the construction term in Kunz model is proportional to $P - P_v$, while Sauer's source term is proportional to $\sqrt{P - P_v}$, and consequently Sauer's model needs larger values to perform the same production. In both models some production also appears close to the surface of the cavity.

The destruction term is located along the surface of the cavity. This is especially clear in Kunz' model since the destruction term is defined as a polynomial of the volume fraction which has its maximum at $\gamma=1/3$. The extension of the destruction term is similar in both models, but the peak value is different, Sauer's model has a slightly higher peak value than Kunz' model. It is harder to directly compare Kunz' and Sauer's destruction since they are based on different equations, but qualitatively they act in a similar way.

Validation of the Twist11 case

Even though 2D experiments are very useful and simple, they can also be very complicated to compare with 2D computations. A 2D hydrofoil has an extension in the spanwise direction in which the shedding can be intermittently and random, yielding a 3D flow field which is not directly comparable with a 2D computation. The computations can be extended to 3D, but then the intermittency and randomness is still a problem which can be hard to overcome. Instead a twisted 3D foil can be used and compared with a 3D computation. On a twisted 3D hydrofoil the shedding mechanism depends on the spanwise loading and the influences of the outer walls can be decreased, since the cavity can be positioned away from these. This allows for observations of controlled 3D effects and the shedding mechanism is somewhat simplified.

The 3D hydrofoil used here is referred to as the Twist11 hydrofoil, see Fig 7. This hydrofoil is generated from a NACA0009 profile with an alternating angle of attack. The largest angle of attack is located at the mid section while the lowest angle of attack is located at the walls. The number 11 in the name of the hydrofoil, Twist11, refers to the angle of attack which differs between the centerplane and the outer edges with 11 degrees, described by third degree polynomial function. The spanwise extent of the wing 300 mm and the chord length is 150 mm. With this hydrofoil an isolated sheet cavity is created around the centre plane and the hydrofoil is lightly loaded to suppress any interaction with the tunnel boundary layer. The three-dimensionality of the cavity, and the hydrofoil, creates a reentrant flow which at some instances is directed sideways at a 90 degree angle with the free flow. This side entrant flow collects fluid towards the centre where the gathered fluid pierces the cavity and leaves a detached cavity which rolls-up into a hairpin. An upstream reentrant jet is now formed, which gathers fluid from the side entrant flow and is directed towards the leading edge of the hydrofoil. The reentrant flow breaks up the sheet around the centerplane on its way towards the leading edge. When the cavity hits the leading edge it is directed towards the outer side of the cavity and a new cavity is started. The cavity which has rolled up into a hairpin vortex is transported towards the trailing edge of the hydrofoil where it finally collapses. After the shedding of the main centre hairpin vortex several smaller vortices is shed from alternating sides of the centerplane until a new cycle is completed.

Setup

To be able to simulate at least some of these highly complicated flow phenomena a high resolution computational mesh is needed. For this purpose three different meshes have been produced, with 600,000, 2,000,000 and 3,000,000 cells respectively. To save cells only half of the domain is modelled, using a symmetry plane at the centre plane. We will here focus on the results obtained with Kunz' mass transfer model on the grid with 3,000,000 cells. The computational domain, mirrored in the centre plane, can be seen in figure 7. The angle of attack of the hydrofoil differs from -2^o at the wall to 9^o at the centre plane. The experimental study on this hydrofoil is not yet published, but an experimental study with an almost similar twisted hydrofoil, Twist8, is published by Foeth and Terwisga [4,5]. Twist8 has the same profile as the Twist11 hydrofoil, but with a lower deviation in angle of attack, 0 degree to 8 degree, Computations have also been performed on the described geometry, Schnerr [17], using a compressible Euler solver.

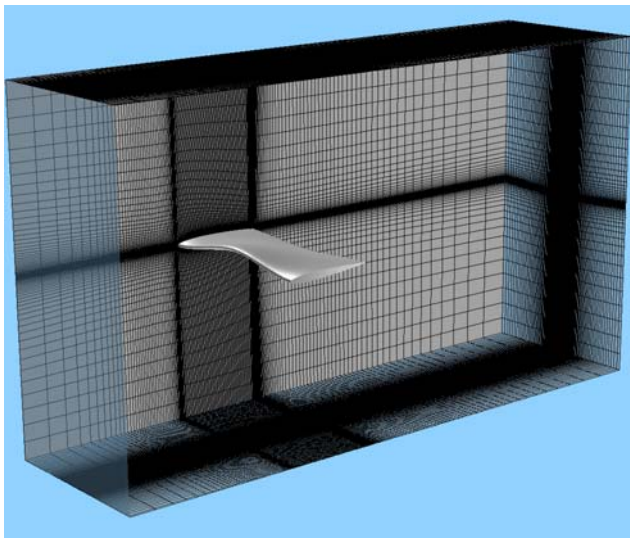

Figure 7. Computational domain for the twisted hydrofoil, the mesh contains 3,000,000 cells. This domain is mirrored in the centerplane for clarification, only half of the domain is used in the computations.

Cavitation phenomena

In the present numerical simulations of steady inflow cases the cavitation sources are gradually turned on during approximately 1 ms. The first sheet cavity that grows becomes very smooth and symmetric. This development may be influenced by the way in which the cavity sources are turned on as well as the fact that there are no vapour voids downstream, as residues from a cavity of a previous cavitation cycle. When the first cavity, by the reentrant jet, is terminated from the leading edge region and advected downstream, the next sheet starts growing. This second sheet behaves less smooth and symmetric, and its development is supposed to be noticeably controlled by the disturbances of the local flow induced by the residue void from the first sheet. This void is now, simultaneously with the growth of the second sheet, rotating and mowing downstream, and finally it leaves the foil and disappears in the region of higher pressure. Detailed velocity and pressure plots indicate existence of significant disturbances of the flow close to the growing second sheet.

It is noted in passing that Wikström and co-workers [20] record also the first cavity in a transient motion of the foil in the ILES simulations as well as in an experiment. The first growth was described reasonably well but due to the preliminary character of the experiment as well as the simulation, it was not at that time possible to make reliable observations beyond the growth of the first sheet. From an academic point of view an advantage of the first cavitation cycle is that the behaviour of the cavitation model is well defined and relatively easy to evaluate, and as pointed out above, this part can also be important in for example certain propeller cases. The possibly following cavitation cycles become more variable and disturbed by interaction from co-existing shed voids, conditions that are typical for water turbines as well as propellers.

Figures 8a-11a show the extension of the cavity as an iso-surface of the volume fraction $\gamma = 0.5$, and the direction of the shear stress of the surface of the wing. Figures 8b-11b show the same iso-surface, in combination with the vector field on the centre plane and the vector field in the first cell layer above the surface. The vector fields are coloured with the volume fraction γ. $\gamma = 0$ (white) corresponds to pure vapour and $\gamma = 1$ (blue) corresponds to pure liquid.

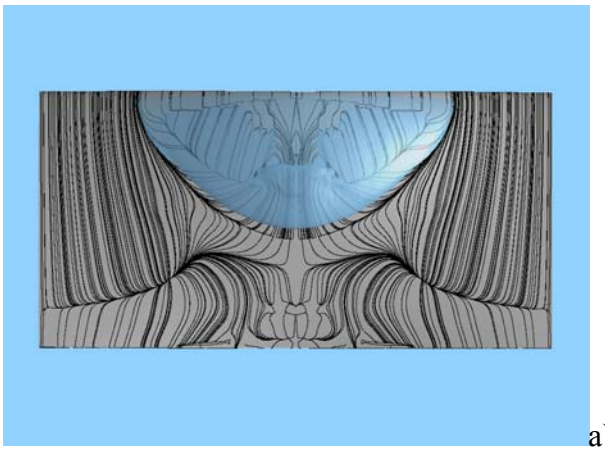
a)
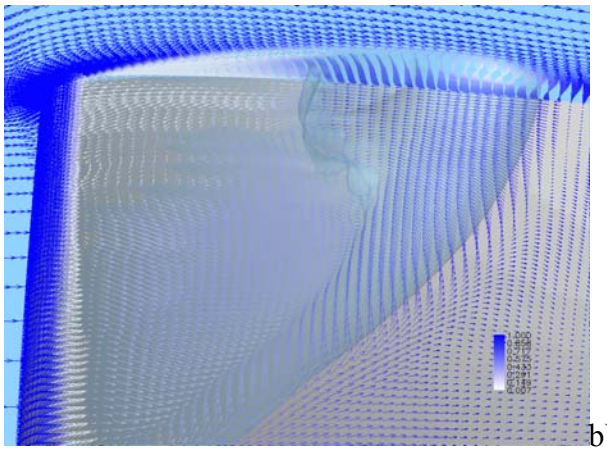
b)

Figure 8. The first cavitation cycle. The cavity has grown to its maximum size and the side jets are fully active to collect fluid towards the closure.

In Fig. 8 the first cavity has grown to its maximum extension regarding cavity length and width. The side entrant jets are clearly visible by the surface shear stress, collecting fluid towards the centre. This fluid gathers to a thicker reentrant jet and forms a closure which snaps of a first cavity in a hairpin vortex. From the shear stress restricting lines it is visible that a massive recirculation zone has developed close to the trailing edge, this recirculation zone is only very small, located close to the centerplane, for the fully wetted flow field.

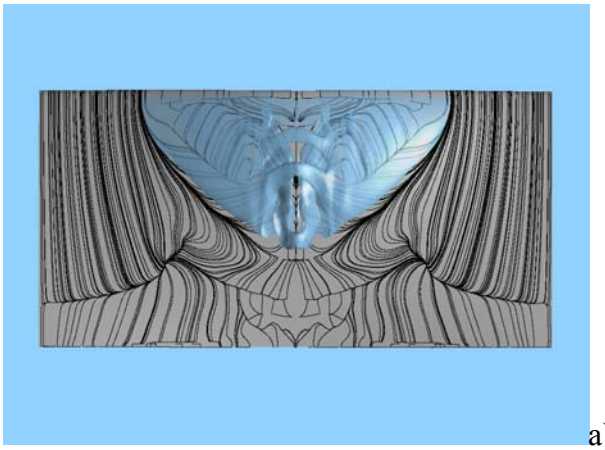
a)
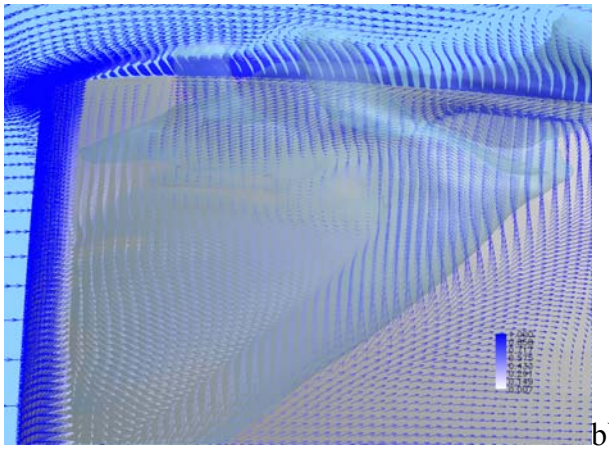
b)

Figure 9. The side jets have formed a reentrant jet which has reached to the leading edge.

In Fig. 9 the re-entrant jet has formed at the first closure and it is convected towards the leading edge, in opposite direction to the outer flow. The jet leaves several hairpin vortices in which the cavity grows stronger due to the high vorticity in these regions. The first hairpin vortex is transported towards the trailing edge of the wing and starts to break off from the main cavity.

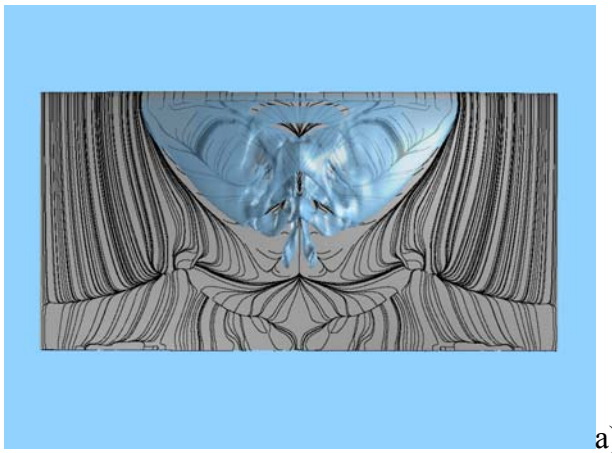
a)
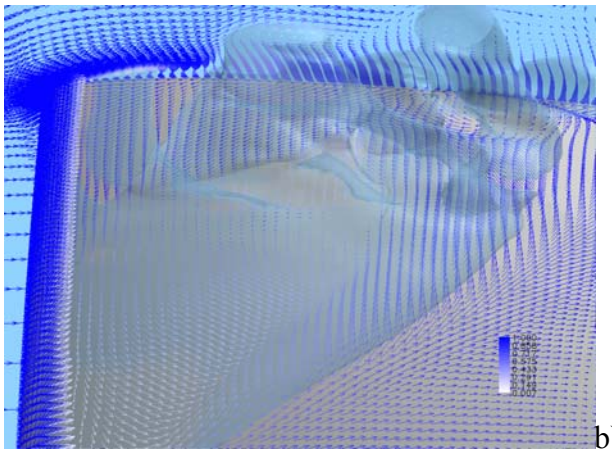
b)

Figure 10. The cavity in the hairpin vortex is being transported into the wake and a new sheet cavity is started.

In Fig. 10 the reentrant jet has hit the leading edge and is directed towards the outer sides of the cavity. The first cavity sheet, which is annihilated by the reentrant jet, is replaced by a new cavity sheet which is growing at the leading edge. The first hairpin vortex cavity is now released from the main cavity and starts to break up and the side entrant jet continually feeds the centre of the cavity with new fluid.

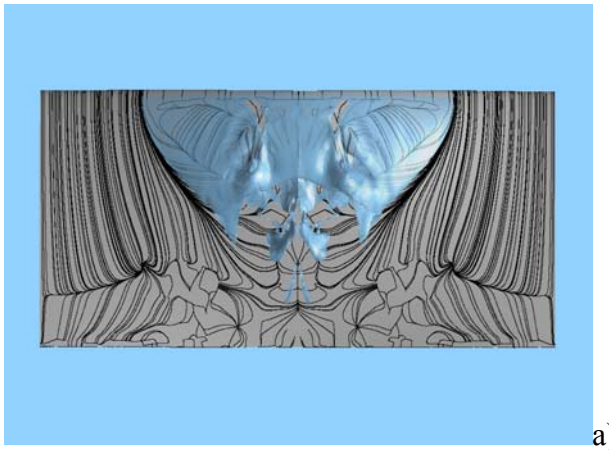
a)
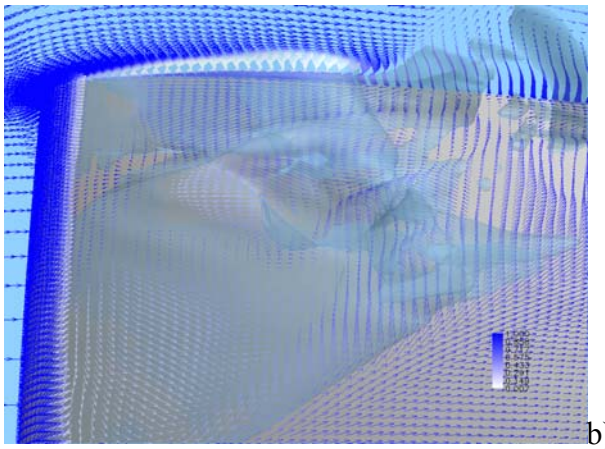
b)

Figure 11. The secondary vortices are being shed and the new cavity sheet is almost fully developed.

After the first shedding cycle a new sheet cavity is created close to the centre region of the hydrofoil, see Fig. 11. This cavity is clearly affected by the first reentrant jet and becomes somewhat thinner than the previous cavity sheet, but the gathering of fluid from the side jet, which forms the reentrant jet, is still very distinct. The new cavity sheet is formed on top of a thin layer of liquid and a much thinner reentrant flow is controlling the shedding of this cavity sheet. But still a new hairpin vortex is shed close to the centre plane. The overall appearance of the cavity is now more realistic than in the first cavitation cycle where the cavity was too steady and smooth. In the experiments at stationary inflow the whole centre region is gathered with bubbles and wavy structures, and these wavy structures now also start to appear in the computation.

Preliminary bubble density distribution from LPT simulations

As mentioned above, the Sauer mass transfer model uses a bubble density, or cavitation nuclei, distribution. Lagrangian Particle Tracking is here used to study the distribution of cavitation

nuclei for the 2D NACA0015 case. The same settings are used, as in the validation of the mass transfer models, but no cavitation modeling is included. Both the unsteady flow and the tracking of the cavitation nuclei are included in the simulations. The cavitation nuclei are randomly injected from a vertical plane upstream the wing at different rates of injection (number of nuclei per time step), and for different cavitation nuclei size. 30 injections (resp. 100) per time step lead to a mean particle density $n_0=4e^8$ (resp. $n_0=1.4e^9$) at the inlet and in all the domain far from the wing. The cavitation nuclei are defined as small bubbles of air (1μm and 50μm) with density $\rho_P=1$ and coefficient of restitution $\varepsilon_w=0.2$. The cavitation nuclei distribution is then obtained from the time average of the number of nuclei per unit volume in each cell. Fig.12 shows the non-uniform cavitation nuclei distribution by highlighting the cells where the density is larger than at the inlet.

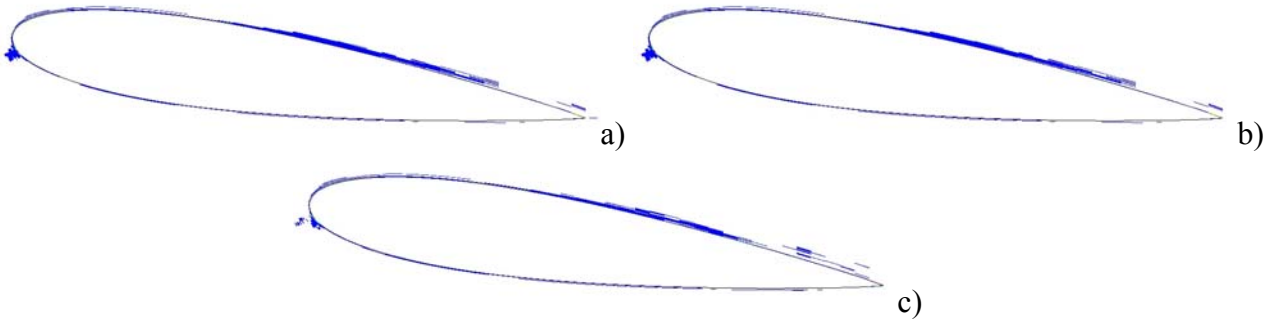

Figure 12: Non-uniform cavitation nuclei distribution. Cells with a larger density than at the inlet are highlighted. a) 30 injections per time step, diameter 1μm. b) 30 injections per time step, diameter 50μm. c) 100 injections per time step, diameter 50μm

All the cases with different rates of injection and different cavitation nuclei sizes give similar results, i.e. an almost constant value of the density in the overall domain, and higher values in certain regions close to the wing where the cavitation nuclei accumulate. The cavitation nuclei density reaches its maximum value at the stagnation point ($n_0 \sim 3e^{11}$), where the reduced velocity prevents the nuclei from flowing downstream. Accumulation is also observed very close to the wing both on the suction and pressure sides, where the low velocity in the boundary layer, and the small vortices near the wall capture the nuclei. One important result is that the nuclei are accumulated in the region of low pressure at the leading edge suction side. An increased cavitation nuclei density in regions of low pressure is likely to affect the inception of cavitation. The next step will be to use these nuclei distributions in a modified Sauer's model and study how the non-homogeneous nuclei content influences cavitation inception and development.

Conclusion

General experiences regarding experimental observation of cavitation concludes that highly resolved numerical predictions of cavitation is necessary to be able to understand the mechanisms of cavitation behaviour better. Even though it is not possible to numerically predict collapses of cavities, general large scale behaviours can be studied to evaluate the risk of destructive collapses, i.e. erosion [1] This kind of early development is what the present cavitation models are able to predict with relatively high accuracy. To be able to better understand this capability both a number of simpler and a number of more advanced validation cases will have to be studied. These validation cases can be used to describe the limitations of the numerical

simulations, and what to expect from the computed results regarding grid resolution, turbulence modelling and other numerical parameters.

The first test case, the 2D NACA0015, is primarily used as a quick parameter test case where properties such as numerical constants, grid resolution, numerical interpolation schemes and mass transfer models can be tested. Even though the spanwise averaging which takes place in a 2D simulation is a strong limitation, many of the features seen from experiments are present. This includes unsteady flow, realistic flow phenomena, well predicted cavity length, realistic behaviour of the reentrant jet and the basic shedding mechanism. The main limitation in this kind of modelling lies in the formulation of the vapour fraction. Using the transport equation for the volume fraction, with the VOF approach, all cavities will be treated as single volume cavities, even if the experiments clearly show a cavity comprised of bubbles. This limitation will affect the development of the subsequent cavity cycles, since the influence on the flow field, and the pressure distribution, will be much different from a convected sheet as compared to a convected bubble cloud.

The second test case, the Twist11 hydrofoil, is a computationally more advanced problem. The cavitating flow over this geometry comprises many of the flow characteristics which occur on e.g. marine propellers and hydraulic turbine runners. This includes features such as periodic shedding of main and secondary cavities in hairpin vortices, side jets and reentrant jets. To be able to predict these phenomena a relatively high resolution of the computational mesh is needed, especially in the spanwise and streamwise directions. The ability to predict this kind of flow structures is very important for predicting the risk of erosion. The experiments performed on the twisted hydrofoil also include controlled shedding frequency using flapped wings in front of the Twist11 hydrofoil. This case is more demanding in meshing and setup of the problem, but for solving the problem the natural frequency will be harder to predict than the controlled frequency.

In total we have shown the capabilities of the described mass transfer methods on two different cases, the NACA0015 and the Twist11 hydrofoil. With the present settings the main features of the cavitating flow field is described and the limitations are explained. Further developments towards a better flow prediction, i.e. sub-grid modelling and wall handling, as well as more mass transfer models will be implemented and tested. We also intend to evaluate these methods on more advanced problems such as propellers and water turbine runners.

The preliminary results from the Lagrangian Particle Tracking simulations show that the cavitation nuclei accumulate at the stagnation point and in the boundary layers. The most important result is that the nuclei are accumulated in the region of low pressure at the leading edge suction side. An increased cavitation nuclei density in regions of low pressure is likely to affect the inception of cavitation. The next step will be to use these nuclei distributions in a modified Sauer's model and study how the non-homogeneous nuclei content influences cavitation inception and development.

Acknowledgement

This work is supported by the EU project VIRTUE under grant 516201, the Rolls Royce UTC at the department of Shipping and Marine Technology at Chalmers, the Swedish Material Administration (FMV) under grant 'MarinLES' and the Swedish Hydropower Centre - SVC. SVC has been established by the Swedish Energy Agency, Elforsk and Svenska Kraftnät together with Luleå University of Technology, The Royal Institute of Technology, Chalmers University of Technology and Uppsala University, www.svc.nu. The authors would also like to acknowledge Dr. Rickard Bensow, Dr. Johan Revstedt and Professor Christer Fureby for fruitful discussions, Professor Yamagushi for communicating the experimental data on the NACA0015 wing profile and Professor Tom van Terwisga and Evert-Jan Foeth for distributing the geometry off the

Twist11 hydrofoil and for discussions regarding the experimental results. The experimental work regarding the Twist11 hydrofoil is sponsored by the Dutch Technology Foundation STW project TSF 6170. Finally Henry Weller is acknowledged for the development of the C++ class library OpenFOAM, used here.

Nomenclature

Symbols

$\mathbf{B}$	Subgrid stress tensor
C	Mass transfer constant
$\mathbf{D}$	Rate-of-strain tensor
D	Diameter
$\mathbf{F}$	Force
R	Bubble radius
$\mathbf{S}$	Viscous stress tensor
$\overline{\mathbf{S}}$	Filtered viscous stress tensor
S	Source term
U	Velocity scale
p	Pressure
$\dot{m}$	Mass transfer term rate
n_0	Specific bubble density
t	Time scale
$\mathbf{v}$	Velocity
$\overline{\mathbf{v}}$	Filtered velocity
$\mathbf{x}$	Position
ε_w	Coefficient of restitution
γ	Volume fraction
ρ	Density
μ	Viscosity

Superscripts and subscripts

$\mathbf{D}$	Drag
$\mathbf{P}$	Particle
dest	Destruction
l	Liquid
n	Particle number
prod	Production
v	Vapour
∞	Free stream value

References

[1] Bark, G., Berchiche, N. and Grekula, M., 2005, “Application of principles for observation and analysis of eroding cavitation - The EROCAV observation handbook”, Department of Naval Architecture and Ocean Engineering, Chalmers University of Technology, Gothenburg

[2] Crowe, C.T., Stock, D.E and Sharma, M.P., 1977, The particle-source-in cell (PSI-CELL) model for gas-droplet flows, ASME, Journal of Fluids Engineering, vol. 99, p. 325-332.

[3] Foeth, E.J. and Terwisga, T., 2006, "The structure of unsteady cavitation. PART II: Applying time-resolved PIV to attached cavitation", Cav2006, Wageningen, The Netherlands

[4] Foeth, E.J., van Doorne, C. W. H., van Terwisga, T. and Wieneke, B., 2006, "Time resolved PIV and flow visualization of 3D sheet cavitation", Experiments in Fluids, 40(4),pp. 503-13

[5] Foeth, E.-J. and Terwisga, T., 2006, "The structure of unsteady cavitation. Part I: Observation of an attached cavity on a three-dimensional hydrofoil", CAV2006, Wageningen, The Netherlands

[6] Fureby, C., Bensow, R. E. and Persson, T., 2005, "Scale similarity revisited in LES ", Turbulence and Shear Flow Phenomena, Williamsburg, USA

[7] Grinstein, F.F., Margolin, L. and Rider, W., 2005, Implicit Large Eddy Simulation: Computing Turbulent Fluid Dynamics, *Cambridge University Press.*

[8] Hill, T. L. (1986). Statistical Thermodynamics, Dover Publications

[9] Hirt, C. and Nicols, B., 1981, Volume of Fluid (VOF) mthod for the Dynamics of Free Boundaries, Journal of Computaional Physics 39(1), pp.210

[10] Hohenberg, P. C. and Halperi,n B. I. (1977). "Theory of dynamic critical phenomena." Reviews of Modern Physics 49(3), pp. 435-79

[11] Kunz, R. Boger, F., Stinebring, D. R., Chyczewski, T. S., Lindau, J. W., Gibeling, H. J., Venkateswaran, S., Govindan, T. R., (2000). "A preconditioned Navier-Stokes method for two-phase flows with application to cavitation prediction." Computers and Fluids 29(8), pp. 849-875.

[12] Merkel, C. L., Feng, J., Buelow, P.E.O. (1998). Computation modelling of the dynamics of sheet cavitaton. 3rd International Symposium on Cavitation. Grenoble, France.

[13] Panton, R. L., 1996, "Incompressible Flow", Wiley-Interscience, New York

[14] Persson, T., Bark, G., Bensow, R. E., Berchiche, N. and Fureby, C., 2006, "Large eddy simulation of the cavitating flow around a wing section", CAV2006, Wageningen, The Netherlands

[15] Sagaut, P., 2001, Large Eddy Simulation for incompressible flows, Berlin Springer Verlag

[16] Sauer, J. (2000). Instationär kaviterende Strömung - Ein neues Modell, baserend auf Front Capturing (VoF) und Blasendynamik. Fakultät fur Maschinenbau Karlsruhe, Universität Karlsruhe. Doktors der Ingenieurwissenschaften.

[17] Schnerr, G. H., 2006, "Shock and wave dynamics of compressible liquid flows with special emphasis on unsteady load on hydrofoils and on cavitation in injection nozzles", CAV2006, Wageningen, The Netherlands

[18] Ubbink, O. (1997). Numerical prediction of two fluid systems with sharp interfaces. Department of Mechanical London, Imperial College of Science, Technology and Medicine. Doctor of Philosophy.

[19] Wikström, N., Bark, G. and Fureby, C., 2003, "Large Eddy Simulation of Cavitating Submerged Objects", The 8th International Conferance on Numerical Ship Hydrodynamics, Busan, Korea

[20]Wikström, N., 2005, "Modeling of Cavitating flow around a Stationary/Moving Wing Profile", 43rd AIAA Aerospace Sciences Meeting, Reno, Nevada

[21] Wilcox, D. C. (1993). Turbulence modelling for CFD, DCW Industries

[22] Wosnik, M., Qiao, Q., Kawakami, D.T. and Arndt, R.E.A., (2005). “Large Eddy Simulation (LES) and time-resolved particle image velocimetry (TR-PIV) in the wake of a cavitating hydrofoil”, FEDSM 2005, Houston, Texas, USA
[23] Yakushiji, R., H. Yamaguchi, et al. (2001). "Investigation for unsteady cavitation and reentrant jet on a foil section." Journal of the society of naval architects of Japan 189.